OPTOMECHANICAL MODULATION TOMOGRAPHY FOR UNGATED COMPRESSIVE CARDIAC LIGHT SHEET MICROSCOPY

François Marelli* *Michael Liebling**,†

**Idiap Research Institute*, CH-1920 Martigny, Switzerland
†*Electrical & Computer Engineering, University of California*, CA 93106 Santa Barbara, USA

ABSTRACT

OptoMechanical Modulation Tomography (OMMT) is a compressed sensing optical microscopy method where measurements are obtained by scanning a light sheet through a sample while modulating its intensity over the course of the camera integration time. Because mechanical scanning is not instantaneous, this method was so far considered unsuitable for imaging dynamic samples. Yet living samples would particularly benefit from the method's reduced light exposure. In this paper we extend OMMT to allow imaging of objects that have a periodic motion, such as the heart in transparent larvae. We derived a method in which measurements are obtained by integrating the space-phase domain along patterned paths. We implemented the reconstruction with an iterative solver, and demonstrated the feasibility of the method based on simulated data of a beating heart. We observed that compression factors up to 8 lead to reliable reconstruction, and that the method is robust to uncertain acquisition start phases. Our results confirm that OMMT can be extended to imaging dynamic samples opening up the possibility to apply this method in experimental settings where low light exposure is desirable.

Index Terms— Computational imaging, fluorescence microscopy, inverse problems, heart

1. INTRODUCTION

OMMT enables 3D compressive light sheet microscopy by acquiring scanned projections with modulated illumination [1, 2]. By reducing the number of images needed to reconstruct a volume, it decreases light exposure, which may reduce photo-damage. However, because scanning is slow, only static objects have been imaged so far with this technique, and it was deemed unsuitable for imaging dynamic objects. More generally, the slowness of depth-scanning is a frequent hurdle to image dynamic samples such as the beating heart, as motion artefacts appear in the measurements.

For periodically moving objects, imaging methods based on scans or projections can nevertheless be employed by use of gated acquisition and fast sampling to reconstruct dynamic volumes. Indeed, when taking images at a single phase with a projection or scanning speed much faster than the dynamics of the sample, the problem becomes similar to reconstructing a still volume. For example, ECG gating is applied in cardiac micro-computed tomography [3], for 4D blood flow Magnetic Resonance Imaging (MRI) [4], and for Optical Coherence Tomography (OCT) with heart pacing [5]. Exploiting space-time sparsity in the data allowed implementing compressed sensing MRI, reducing the amount of ECG-gated acquisitions [6].

Gated imaging requires a complex pipeline to trigger synchronized acquisitions [7], which is not available on all devices. Ungated
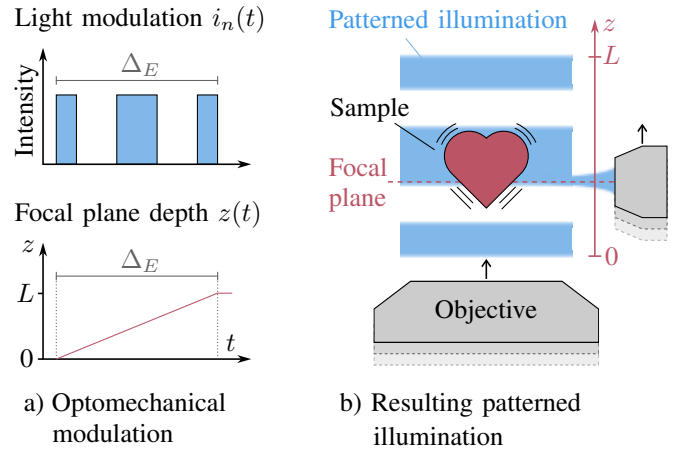

Fig. 1. Overview of OMMT imaging. (a) Optomechanical modulation consists in simultaneously scanning the focus plane in depth and modulating the light intensity. (b) This results in illumination patterns along the depth axis.

methods trade this complex pipeline for retrospective phase estimation algorithms in order to reconstruct 4D data without motion artefacts, with applications in colour Doppler OCT [8] and 4D confocal microscopy [9]. However, these methods require imaging the whole volume and are not suitable for compressed sensing. Moreover, they also assume that the acquisition of a single measurement is much faster than the motion of the sample. This is not achievable with OMMT, as the acquisition speed of the projections is limited by the scanning time of a mechanical stage.

Here, we investigate an ungated method that leverages space-time sparsity to perform compressed 4D sensing based on modulated scanned projections. It expands upon our static version of OMMT [2], introducing an imaging model that includes temporal periodicity to reconstruct dynamic samples such as a beating heart. We characterize its compression abilities on synthetic data, and evaluate its robustness to errors in the retrospective phase estimation.

2. METHOD

We briefly recall the principles of OMMT, which relies on the acquisition of modulated pseudo-projections that combine temporal illumination modulation with depth scanning on a light sheet microscope [10]. During a full camera exposure time Δ_E, the mechanized focus stage moves at a constant speed v in depth while the intensity of the illumination varies following a chosen temporal modulation

function. This simultaneous optomechanical modulation generates a patterned illumination along depth, as shown in Fig. 1. The camera performs an optical integration during the exposure time, which yields the modulated pseudo-projection. This process can be repeated any number of times with different illumination modulations, generating a set of measurements from which it is possible to reconstruct the original three-dimensional (3D) object, which has so far been assumed to be static.

2.1. Forward model with time periodicity

In this paper we consider a periodically moving dynamic 3D object, $f(x, y, z, \theta)$, with x, y, z the horizontal, vertical, and focus axes respectively. The sample shape varies over time according to its phase θ, repeating with period 2π:

$$f(x, y, z, \theta) = f(x, y, z, \theta + k\, 2\pi), \ \forall k \in \mathbb{Z}. \quad (1)$$

This phase evolves linearly with time, $\theta(t) = \omega t$, with ω the angular frequency. In our proposed dynamic OMMT method, we acquire N pseudo-projections $p_n(x, y)$ ($n = 1, \ldots, N$) using illumination modulation functions $i_n(t)$, according to:

$$p_n(x, y) = \int_0^{\Delta_E} [f * h](x, y, vt, \omega(t + t_{i,n}))\, i_n(t)\, \mathrm{d}t, \quad (2)$$

where $h(x, y, z)$ is the Point Spread Function (PSF) of the microscope, and $t_{i,n}$ is the arbitrary initial time at which the acquisition of projection n starts. We use $*$ to denote a 3D spatial convolution operator, applied on the x, y, z dimensions.

As the set of modulation functions, we use a subset of a Hadamard basis, which we chose for the simplicity of implementation and successful use in multiple compressed imaging applications [11]. Starting from a Hadamard matrix $\mathbf{H}_M$ of order M in which we set all -1 values to 0 (resulting in a matrix whose values are either 0 or 1) the illumination functions are obtained through random row selection:

$$i_n(t) = \mathbf{H}_M[m(n), j] \qquad \text{s.t. } j - 1 \le \frac{Mt}{\Delta_E} < j, \quad (3)$$

where $m : \{1, \ldots, N\} \to \{1, \ldots, M\}$ is a mapping that selects a row of $\mathbf{H}_M$ with uniform probability.

We have shown previously that Eq. (2) can be simplified by using a 1D PSF model $h'(z) = h(0, 0, z)$, which still accurately represents the system [2]. Using this approximation, the forward model becomes a 1D expression at any location (x, y). For the rest of this paper, we will focus on what happens at an arbitrarily chosen position (x', y') in space. Indeed, solving this simpler 2D (depth + time) problem allows reconstructing the whole 4D sample (3D + time) simply by combining the results at any desired coordinate (x', y') as depicted in Fig. 2(a). Eq. (2) then becomes:

$$p'_n = \int_0^{\Delta_E} [f' \circledast h'](vt, \omega(t + t_{i,n}))\, i_n(t)\, \mathrm{d}t, \quad (4)$$

where $f'(z, \theta) = f(x', y', z, \theta)$ represents the values of the object along the selected (x', y') pillar, and $p'_n = p_n(x', y')$ is the projection at that same coordinate. We use $\circledast$ to describe a 1D spatial convolution operator applied on the z dimension.

We reformulate the line integral in Eq. (4) by capturing its linear path with a delta ridge distribution in depth-phase space:

$$\int \phi(vt, \omega t)\, \mathrm{d}t = \iint \phi(z, \theta)\, \delta\left(\frac{z}{v} - \frac{\theta}{\omega}\right)\, \mathrm{d}z\mathrm{d}\theta \quad (5)$$
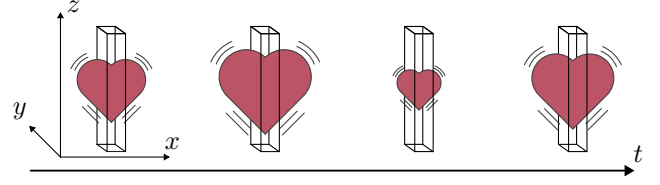
a) Selected (x', y') pillar through time
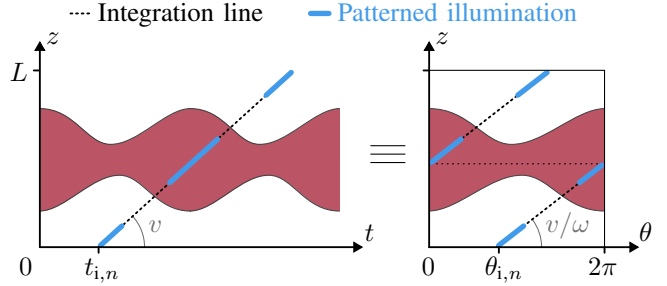
b) Corresponding kymograph and sampling

Fig. 2. Representation and sampling of the data. (a) We study a single pillar through time, located at coordinates (x', y'). (b) We plot the values on this pillar using a space-time kymograph (left), or the equivalent space-phase kymograph with phase wrapping (right). The sampling function consists in applying the light pattern along the integration line.

(with ϕ an arbitrary function) and further simplify Eq. (4) by expanding the convolution and reordering the integrals:

$$p'_n = \int_0^L \int_{\theta_{i,n}}^{\omega\Delta_E + \theta_{i,n}} \int_{-\infty}^{\infty} f'(u, \theta)\, h'(u - z)\, \mathrm{d}u$$
$$\delta\left(\frac{z}{v} - \frac{\theta - \theta_{i,n}}{\omega}\right) i_n\left(\frac{\theta - \theta_{i,n}}{\omega}\right)\, \mathrm{d}\theta\mathrm{d}z \quad (6)$$

$$= \int_\theta \int_u \int_z h'(u - z)\, \delta\left(\frac{z}{v} - \frac{\theta - \theta_{i,n}}{\omega}\right) \mathrm{d}z$$
$$f'(u, \theta)\, i_n\left(\frac{\theta - \theta_{i,n}}{\omega}\right)\, \mathrm{d}u\mathrm{d}\theta \quad (7)$$

$$= \int_\theta \int_u h'\left(u - \frac{v}{\omega}(\theta - \theta_{i,n})\right)$$
$$f'(u, \theta)\, i_n\left(\frac{\theta - \theta_{i,n}}{\omega}\right)\, \mathrm{d}u\mathrm{d}\theta, \quad (8)$$

in which $\theta_{i,n} = \omega t_{i,n}$ is the initial phase corresponding to the start of the acquisition. Finally, we define $g'_n(z, \theta)$ as the sampling function by shifting the PSF along the integration line and multiplying it with the light modulation:

$$g'_n(z, \theta) = h'\left(z - \frac{v}{\omega}(\theta - \theta_{i,n})\right)\, i_n\left(\frac{\theta - \theta_{i,n}}{\omega}\right), \quad (9)$$

such that Eq. (8) becomes:

$$p'_n = \int_{\theta_{i,n}}^{\omega\Delta_E + \theta_{i,n}} \int_0^L f'(u, \theta)\, g'_n(u, \theta)\, \mathrm{d}u\mathrm{d}\theta. \quad (10)$$

In Fig. 2(b), we visualize the function $f'(z, \theta)$ as a kymograph and the integration path that results from the trajectory of the focus stage
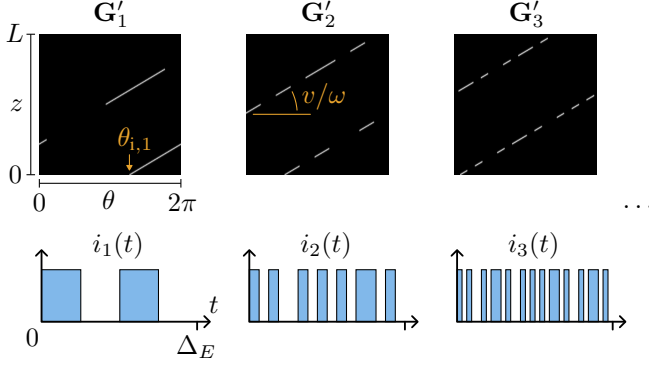
Fig. 3. Examples of sampling matrices and their associated light modulation patterns. Each of these matrices $\mathbf{G}'_n$ corresponds to the acquisition of pseudo-projection p'_n. Flattened and stacked, they constitute the imaging operator $\mathbf{G}'$.

through space and heart beat phase as a line, over which we apply the patterned illumination yielding sampling function g'_n. Due to the periodicity of the system, it is equivalent to represent the values in a space-phase kymograph, wrapping the phases between 0 and 2π.

When discretized for all n, Eq. (10) becomes a linear model:

$$\vec{p} = \mathbf{G}' \vec{f}' + \vec{\epsilon}, \tag{11}$$

where $\vec{f}' \in \mathbb{R}^{DT}$ is the vector containing the sampled values of f', with D sampling steps in depth and T steps in time, $\mathbf{G}' \in \mathbb{R}^{N \times DT}$ is the matrix operator corresponding to the multiplication with all the g'_n and the integration. $\vec{p} \in \mathbb{R}^N$ is the vector containing the projections, and $\vec{\epsilon} \in \mathbb{R}^N$ is the measurement noise. To perform compressed sensing, we acquire a number of projections lower than the number of unknowns, $N \leq DT$, and denote by C the compression factor, $C = DT/N \geq 1$. Each row in $\mathbf{G}'$ is a flattened matrix $\mathbf{G}'_n$ resulting from the discretization of the corresponding sampling function g'_n, illustrated in Fig. 3.

Building the $\mathbf{G}'_n$ matrices requires knowing the arbitrary acquisition phases $\theta_{i,n}$ and the angular frequency ω of the signal. Computing these phases could be done in post-processing by using, e.g. the Paired Alternating AcQuisitions (PAAQ) imaging technique [2]. Note that there is no constraint on the values of $\theta_{i,n}$, thus this method does not require any gating to the heart beat *during* acquisition.

2.2. Inverse problem

To reconstruct $\vec{f}'$ from the measurements, we must solve the linear inverse problem corresponding to Eq. (11). Since the number of measurements is lower than the reconstruction unknowns, this problem is ill-posed and requires the use of regularization to obtain a satisfactory solution. For compressed sensing, this inverse problem is commonly expressed as an energy minimization task [11]:

$$\vec{f}^* = \underset{\vec{f}^* \in \mathbb{R}^{DT}}{\arg\min} \; \mathcal{C}\left(\vec{p}, \mathbf{G}' \vec{f}\right) + \lambda_z \, \mathcal{R}_z\left(\vec{f}\right) + \lambda_\theta \, \mathcal{R}_\theta\left(\vec{f}\right), \tag{12}$$

where $\mathcal{C}$ is a squared ℓ_2 data consistency loss, and $\mathcal{R}_z$ and $\mathcal{R}_\theta$ are Total Variation (TV) regularization terms along the depth and phase axes respectively, with λ_z and λ_θ being hyperparameters that tune the regularization strengths.

TV is a common regularization that aims at reconstructing smooth images while preserving sharp edges, and is based on the

Table 1. Quantitative characterization on synthetic data.

C	1	2	4	8	16	32
PSNR (dB)	21.9	21.9	21.4	20.3	18.0	13.1

assumption that the spatial gradient of the object is sparse [12]. We penalize it separately for the depth and phase axes as they represent different domains. To match the periodicity of the problem, we use periodic boundary conditions for $\mathcal{R}_\theta$.

We solve Eq. (12) using the alternating direction method of multipliers (ADMM [13]), which iteratively alternates between minimizing $\mathcal{C}$ and the regularization terms. We used the scientific imaging library SCICO [14] implementation, which is efficient and directly applicable to Eq. (12).

In order to reliably select good values for the hyperparameters λ_z and λ_θ, we use a criterion based on the data consistency cost, as introduced in our previous works [2]. It consists in applying $\mathcal{C}$ to the solution of the ADMM optimization, truncated to contain only positive values (since light intensity must always be positive). We find the hyperparameters yielding the minimal truncated cost through a loose grid search.

3. EXPERIMENTS

We used our model developed for cardiac imaging simulation [15] to generate a synthetic sample consisting of a hollow ellipsis traversed by a contraction wave. We emulated acquisition with an OpenSPIM device [16] via a dedicated simulation framework [17] and using a Gaussian beam model for the PSF [18]. We corrupted the data with shot noise modelled by sampling a Poisson distribution after rescaling the measurements to a maximum photon count of 10^4, and quantized the result to 12 bits to emulate a digital camera.

For the sampling operator, we used a uniform distribution to select the initial phases $\theta_{i,n}$ between 0 and 2π. We set $\frac{2\pi v}{L\omega} = 0.4$, meaning that the stage covers 40% of the scanning length over one full period of the signal. This corresponds to acquiring scans over an exposure time $\Delta_E = 1\,\mathrm{s}$, with a cardiac frequency set to $2.5\,\mathrm{Hz}$. We chose these parameters to match that of the zebrafish heart at the larval stage which lies between $2\,\mathrm{Hz}$ to $3\,\mathrm{Hz}$ [19].

We set the reconstruction resolution as $D = 64$ and $T = 50$, and used $M = 32$ to generate the Hadamard modulation. We used the Peak Signal-to-Noise Ratio (PSNR) to quantify the accuracy of the reconstructed images, and repeated each experiment 5 times with different random seeds to obtain averaged results and derive confidence intervals.

We first characterized the performance of our method against the compression factor used for acquisition, using an uncompressed acquisition ($C = 1$) as the reference. Table 1 shows that there is little accuracy drop (less than $1\,\mathrm{dB}$) for low compression factors $C \leq 4$. The performance degrades for higher compressions, with a drop of over $4\,\mathrm{dB}$ for $C \geq 16$ (corresponding reconstructions in Fig. 4). At $C = 32$, the object is still visible, but is strongly distorted.

Since the phase estimates used to build $\mathbf{G}'$ may not be accurate in practice, we investigated what effect this may have on the reconstruction performance. Prior to reconstruction, we added Gaussian noise to the phases as if they had been obtained through inaccurate estimates. Table 2 shows the accuracy of our method for increasing levels of noise in the phases, measured for $C = 4$. With less than 1% phase error—a level of phase estimation accuracy achievable us-
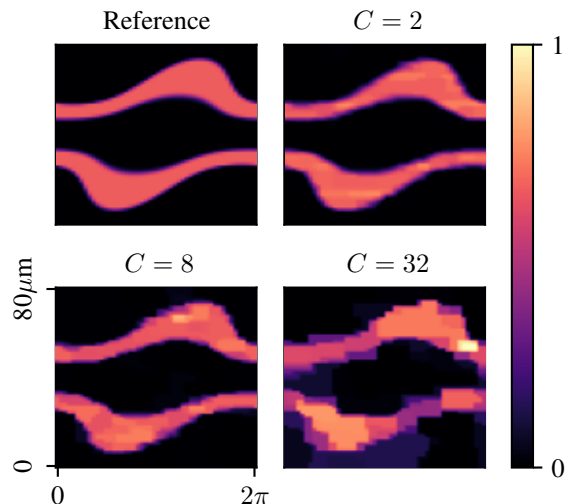
Fig. 4. Obtained reconstructions for different compression factors. The results for $C = 32$ contain strong aberrations, corresponding to the $8\,\mathrm{dB}$ PSNR drop.

Table 2. Robustness to errors in the sampling phase estimates.

Phase error (% of period)	0	0.5	1	2	4
PSNR (dB)	21.4	21.1	19.9	18.5	16.2

ing a sorting-based phase estimation method [15]—the reconstructions are still reliable with a performance drop lower than $1\,\mathrm{dB}$.

4. CONCLUSIONS

We have introduced an ungated OMMT compressive imaging method for studying periodically moving objects. We have derived a forward model that factors in the temporal periodicity of the problem, and used it to implement an ADMM algorithm for the reconstruction of the 4D data split into many 2D problems. Using simulated samples, we characterized the performance of our method with respect to the compression factor, and showed that it gives reliable results for compressions as high as 8. We tested the robustness of our method to errors in the ungated phase estimates, showing that the accuracy drop is minimal at the typical precision offered by retrospective phase estimation. We provide code for reproducing our results at https://github.com/idiap/cbi_toolbox.

5. COMPLIANCE WITH ETHICAL STANDARDS

This numerical simulation study required no ethical approval.

6. ACKNOWLEDGMENTS

7. REFERENCES

[1] M. Woringer, X. Darzacq, C. Zimmer, and M. Mir, "Faster and less phototoxic 3D fluorescence microscopy using a versatile compressed sensing scheme," *Opt. Express*, vol. 25, no. 12, pp. 13 668–13 683, 2017.

[2] F. Marelli and M. Liebling, "Efficient compressed sensing reconstruction for 3D fluorescence microscopy using OptoMechanical Modulation Tomography (OMMT) with a 1+2D regularization," *Opt. Express*, vol. 31, no. 20, pp. 31 718–31 733, 2023.

[3] T. Sera *et al.*, "Development of high-resolution 4D in vivo-CT for visualization of cardiac and respiratory deformations of small animals," *Physics in Medicine & Biology*, vol. 53, no. 16, p. 4285, 2008.

[4] M. Markl, A. Frydrychowicz, S. Kozerke, M. Hope, and O. Wieben, "4D flow MRI," *J. Magn. Reson. Imag.*, vol. 36, no. 5, pp. 1015–1036, 2012.

[5] M. W. Jenkins *et al.*, "4d embryonic cardiography using gated optical coherence tomography," *Opt. Express*, vol. 14, no. 2, pp. 736–748, 2006.

[6] S. G. Lingala and M. Jacob, "A blind compressive sensing framework for accelerated dynamic MRI," in *2012 9th IEEE International Symposium on Biomedical Imaging (ISBI)*. IEEE, 2012, pp. 1060–1063.

[7] J. M. Taylor, J. M. Girkin, and G. D. Love, "High-resolution 3D optical microscopy inside the beating zebrafish heart using prospective optical gating," *Biomed. Opt. Express*, vol. 3, no. 12, pp. 3043–3053, 2012.

[8] S. Yazdanfar, M. D. Kulkarni, and J. A. Izatt, "High resolution imaging of in vivo cardiac dynamics using color doppler optical coherence tomography," *Opt. Express*, vol. 1, no. 13, pp. 424–431, 1997.

[9] M. Liebling, A. S. Forouhar, M. Gharib, S. E. Fraser, and M. E. Dickinson, "Four-dimensional cardiac imaging in living embryos via postacquisition synchronization of nongated slice sequences," *J. Biomed. Opt.*, vol. 10, no. 5, p. 054001, 2005.

[10] J. Huisken, J. Swoger, F. Del Bene, J. Wittbrodt, and E. H. Stelzer, "Optical sectioning deep inside live embryos by selective plane illumination microscopy," *Science*, vol. 305, no. 5686, pp. 1007–1009, 2004.

[11] G. Calisesi, A. Ghezzi, D. Ancora, C. D'Andrea, G. Valentini, A. Farina, and A. Bassi, "Compressed sensing in fluorescence microscopy," *Prog. Biophys. Mol. Biol.*, vol. 168, pp. 66–80, 2022.

[12] L. I. Rudin, S. Osher, and E. Fatemi, "Nonlinear total variation based noise removal algorithms," *Physica D*, vol. 60, no. 1, pp. 259–268, 1992.

[13] S. Boyd, N. Parikh, E. Chu, B. Peleato, and J. Eckstein, "Distributed optimization and statistical learning via the alternating direction method of multipliers," *Found. Trends Mach. Learn.*, vol. 3, no. 1, pp. 1–122, 2011.

[14] T. Balke, F. Davis, C. Garcia-Cardona, S. Majee, M. McCann, L. Pfister, and B. Wohlberg, "Scientific computational imaging code (SCICO)," *J. Open Source Softw.*, vol. 7, no. 78, p. 4722, 2022.

[15] F. Marelli, A. Ernst, N. Mercader, and M. Liebling, "PAAQ: Paired Alternating AcQuisitions for virtual high frame rate multichannel cardiac fluorescence microscopy," *Biological Imaging*, pp. 1–26, 2023.

[16] P. G. Pitrone *et al.*, "OpenSPIM: an open-access light-sheet microscopy platform," *Nat. Methods*, vol. 10, no. 7, pp. 598–599, 2013.

[17] F. Marelli and M. Liebling, "Optics versus computation: Influence of illumination and reconstruction model accuracy in focal-plane-scanning optical projection tomography," in *2021 IEEE 18th International Symposium on Biomedical Imaging (ISBI)*, 2021, pp. 567–570.

[18] A. K. Trull, J. van der Horst, W. J. Palenstijn, L. J. van Vliet, T. van Leeuwen, and J. Kalkman, "Point spread function based image reconstruction in optical projection tomography," *Phys. Med. Biol.*, vol. 62, no. 19, p. 7784, 2017.

[19] K. Baker, K. S. Warren, G. Yellen, and M. C. Fishman, "Defective pacemaker current in a zebrafish mutant with a slow heart rate," *Proc. Natl. Acad. Sci. U.S.A.*, vol. 94, no. 9, pp. 4554–4559, 1997.